Frontiers of Physics
https://doi.org/10.1007/s11467-018-0845-4
Front. Phys.
14(1), 013601 (2019)

RESEARCH ARTICLE

Enhancing the thermoelectric performance of Bi_2S_3: A promising earth-abundant thermoelectric material

Ye Chen[1], Dongyang Wang[1], Yuling Zhou[2], Qiantao Pang[3], Jianwei Shao[4], Guangtao Wang[5], Jinfeng Wang[5], Li-Dong Zhao[1,†]

[1] *School of Materials Science and Engineering, Beihang University, Beijing 100191, China*
[2] *AVIC SAC Commercial Aircraft Co. Ltd., Shenyang 110034, China*
[3] *Liaoning Tieling Sales Branch, Petro China Co. Ltd., Tieling 112000, China*
[4] *Shenyang Liming Areo-Engine Co. Ltd., Shenyang 110043, China*
[5] *College of Physics and Materials Science, Henan Normal University, Xinxiang 453007, China*
Corresponding author. E-mail: [†] *zhaolidong@buaa.edu.cn*
Received July 8, 2018; accepted July 26, 2018

Recently, bismuth sulfide (Bi_2S_3) has attracted much attention in the thermoelectric community owing to its abundance, low cost, and advanced properties. However, its poor electrical transport properties have prevented Bi_2S_3 devices from realizing high thermoelectric performance. In this work, our motivation is to decrease the large electrical resistivity, which is recognized as the origin of the low ZT value in undoped Bi_2S_3. We combined melting and spark plasma sintering (SPS) in a continuous fabrication process to produce $Bi_2S_{3-x}Se_x$ (x = 0, 0.09, 0.15, 0.21) and $Bi_2S_{2.85-y}Se_{0.15}Cl_y$ (y = 0.0015, 0.0045, 0.0075, 0.015, 0.03) samples. Our results show that Se alloying at S sites can narrow the band gap and activate intrinsic electron conduction, leading to a high power factor of $\sim$ 2.0 $\mu W \cdot cm^{-1} \cdot K^{-2}$ at room temperature in $Bi_2S_{2.85}S_{0.15}$, about 100 times higher than that of undoped Bi_2S_3. Moreover, our further introduction of Cl atoms into the S sites resulted in a second-stage optimization of carrier concentration and simultaneously reduced the lattice thermal conductivity, which contributed to a high ZT value of $\sim$ 0.6 at 723 K for $Bi_2S_{2.835}Se_{0.15}Cl_{0.015}$. Our results indicate that high thermoelectric performance could be realized in Bi_2S_3 with earth-abundant and low-cost elements.

Keywords thermoelectric, Bi_2S_3, carrier concentration, lattice thermal conductivity

1 Introduction

Today, the shrinking supply of fossil fuels and environmental pollution have become inevitable problems for social and economic development. The thermoelectric effect, which can realize a direct and reversible conversion between heat and electricity without any pollution or noise, has been providing new solutions for electronic cooling and power generation, particularly from industrial waste heat [1]. The efficiency of the conversion from heat to electric power is determined by the dimensionless figure of merit $ZT = (S^2\sigma/\kappa)T$, where S, σ, κ, and T are the Seebeck coefficient, electrical conductivity, thermal conductivity and temperature in Kelvin, respectively [2–4]. Clearly, to realize a high ZT value, the power factor ($PF = S^2\sigma$) should be larger and the thermal conductivity should be smaller [5, 6].

Bi_2Te_3 compounds are most commonly applied for thermoelectric power generation and electronic cooling around room temperature; however, Te is a scarce element in the crust of the earth. Hence, the price of Te is likely to rise sharply if Te-containing thermoelectric materials reach mass markets. A broad search for more inexpensive alternatives is therefore warranted. It is worth noting that S is an alternative to Te since they belong to the same family, and S is quite abundant in the earth's crust [7]. Therefore, Te-free Bi_2S_3-based thermoelectric materials have attracted great interest due to the high abundance of S ($\sim$480 ppm) in comparison with Te ($\sim$0.001 ppm) [8].

Even though Bi_2S_3 possesses a large Seebeck coefficient and surprisingly low thermal conductivity [9, 10], its large electrical resistivity results in a low ZT value of $\sim$0.05 at room temperature [10]. Much effort has been devoted to enhancing the thermoelectric performance of the Bi_2S_3 system. On the one hand, the electrical transport properties, namely the power factor (PF), can be improved by optimizing the carrier concentration via Ag/Cu/Sb doping into Bi sites [9, 11–13] or Cl/Br/I doping into Cl sites [11, 14–16]. On the other hand, the thermal conductivity could be considerably reduced through nanostructuring

[12, 17].

Liu *et al.* conducted a systematic study of the Bi_2Te_3–Bi_2Se_3–Bi_2S_3 system, and found that the electrical conductivity of Bi_2S_3 could be significantly improved through alloying 1/3 Se in the S sites, and a peak ZT value of ∼0.8 could be achieved at 773 K for Bi_2SeS_2 [18]. This has motivated us to re-investigate Bi_2S_3 with the aim of reducing the Se-alloying fraction in Bi_2S_3 while still maintaining high thermoelectric performance. In this study, to optimize the carrier concentration of undoped Bi_2S_3, we successively alloyed Se and doped Cl into S sites by a melting and SPS synthesis process. Our investigation indicates that Se alloying can narrow the ∼1.30 eV band gap of Bi_2S_3 [19, 20] and Cl doping could greatly improve both the carrier concentration and carrier mobility, resulting in a peak ZT value of ∼0.6 at 723 K for $Bi_2S_{2.835}Se_{0.15}Cl_{0.015}$. Our results show that high-performance Bi_2S_3 could be realized through Se alloying and Cl doping into S sites instead of alloying a large amount of Se.

2 Experimental

Samples synthesis: Reagent chemicals were used as obtained: Bi chunk (99.99%, Trillion Metals), S piece (99.99%, Aladdin), Se chunk (≥99.999%, Aladdin) and $BiCl_3$ powder (99.95%, Macklin). Ingots (∼12 g) with nominal compositions of $Bi_2S_{3-x}Se_x$ (x = 0, 0.09, 0.15, 0.21) and $Bi_2S_{2.85-y}Se_{0.15}Cl_y$ (y = 0, 0.0015, 0.0045, 0.0075, 0.015, 0.03) were synthesized by vacuum sealed tube reaction. Appropriate ratios of high purity starting materials of Bi, S, Se and $BiCl_3$ were loaded in quartz tubes and sealed under high vacuum (∼10^{-4} Torr). The tubes were slowly heated up to 723 K over 12 h, soaked at this temperature for 10 h, then heated again up to 1133 K (10 K higher than the melting point of Bi_2S_3), soaked at this higher temperature for 6 h and subsequently cooled to room temperature. The obtained ingots were crushed into fine powders and then densified by spark plasma sintering (SPS) method (SPS-211LX) at 773 K for 5 minutes in a 12.7 mm-diameter graphite die under an axial compressive stress of 50 MPa in vacuum. Some previous works [11, 14] suggest a sintering temperature of 823 K. However, after optimizing the SPS process, we found that density of SPSed pellets are fully dense and a better thermoelectric performance could be achieved when the sintering temperature was selected as 773 K. As shown in Table 1, a high density (>93% of the theoretical value) of samples was obtained.

Electrical transport properties: The SPSed disk-shaped pellets were cut and polished into bars with dimensions 9 mm × 3 mm × 3 mm. The bars coated with a thin layer of boron nitride (BN) protecting instruments were used for simultaneous measurement of the Seebeck coefficient and the electrical conductivity by CTA-3 (Cryoll, China) under a helium atmosphere from room temperature to 773 K (less than or equal to the sintering temperature). The length direction of the sample is parallel to the SPS pressing direction. The uncertainty of the Seebeck coefficient and electrical conductivity measurements is 3%.

The carrier concentration n_H is determined using $n_H = 1/(eRH)$ where the Hall coefficient R_H was measured using the Hall measurement system (Lakeshore H8400) at room temperature with a magnetic field of 1.2 T. The measurement applied a four-contact Hall-bar geometry with both negative and positive polarity for the purpose of Joule resistive errors estimation.

Thermal transport conductivities: The SPSed disk-shaped pellets were cut and polished into square-shaped thin pellets with dimensions 8 mm × 8 mm × 2 mm. The thermal conductivity was calculated by the relationship of $\kappa = D \times C_p \times \rho$, where D, C_p and ρ are the thermal diffusivity, specific heat capacity and sample density. In preparation for measurements of thermal diffusivity (D) using the laser flash method (Netzsch LFA457, Germany), the samples were coated with a thin layer of graphite to minimize errors from the emissivity of the material. The specific heat capacity (C_p) was indirectly derived using a reference sample (Pyroceram 9606) in the range 300–773 K (less than or equal to the sintering temperature). The

Table 1 Sample densities studied in this work.

Samples	Compositions ($Bi_2S_{3-x-y}Se_xCl_y$)	Measured density (g·cm^{-3})	Theoretical density (g·cm^{-3})	Relative density (%)
$x = 0$, $y = 0$%	undoped Bi_2S_3	6.32	6.78	93.22
$x = 0.09$, $y = 0$%	$Bi_2S_{2.91}Se_{0.09}$	6.74	6.78	99.41
$x = 0.15$, $y = 0$%	$Bi_2S_{2.85}Se_{0.15}$	6.65	6.78	98.08
$x = 0.21$, $y = 0$%	$Bi_2S_{2.79}Se_{0.21}$	6.71	6.78	98.97
$x = 0.15$, $y = 0.15$%	$Bi_2S_{2.8485}Se_{0.15}Cl_{0.0015}$	6.69	6.78	98.67
$x = 0.15$, $y = 0.45$%	$Bi_2S_{2.8455}Se_{0.45}Cl_{0.0045}$	6.73	6.78	99.26
$x = 0.1$, $y = 0.75$%	$Bi_2S_{2.8425}Se_{0.75}Cl_{0.0075}$	6.64	6.78	97.94
$x = 0.15$, $y = 1.5$%	$Bi_2S_{2.835}Se_{0.15}Cl_{0.015}$	6.76	6.78	99.71
$x = 0.15$, $y = 3$%	$Bi_2S_{2.82}Se_{0.15}Cl_{0.03}$	6.77	6.78	99.85

density (ρ) was determined with the dimensions and mass of the sample. The thermal diffusivity data were analyzed using a Cowan model with pulse correction. The total uncertainty of the thermal conductivity was estimated to be within 10%, contributed by a 3% of uncertainty for the thermal diffusivity (D), 5% for the specific heat capacity (C_p), and 2% for the sample density (ρ). The combined uncertainty for all measurements involved in the calculation of ZT is around 20%.

Powder X-ray diffraction: Small pieces were cut off from the SPSed samples and then ground into powders with an agate mortar for X-ray powder diffraction. The diffraction patterns were recorded with Cu Kα (λ = 1.5418 Å) radiation in a reflection geometry on an Inel diffractometer operating at 40 kV and 20 mA using a position-sensitive detector.

Band gap measurements: Room temperature optical diffuse reflectance measurements were performed in the 500–1500 nm region on a UV-VIS-NIR Spectrophotometer (SHIMADZU UV-3600 Plus), where $BaSO_4$ was used as a 100% reflectance standard and compactly preloaded into a sample holder before measurements. The instrument is equipped with the ISR-603 integrating sphere. Samples ground into powders were spread on a plat surface compacted with $BaSO_4$ powders. In order to estimate the band gap of samples, the reflectance versus wavelength data given in the diffuse reflectance spectra was converted to absorption data using Kubelka–Munk equations: $\alpha/S = (1-R)^2/(2R)$, where R, α and S represents the reflectance, the absorption and scattering coefficients, respectively.

Density functional theory (DFT) calculations: First-principles calculations within DFT have been performed using the projector-augmented wave (PAW) method [21], as implemented in the Vienna Ab-initio Simulation Package (VASP) [22]. The exchange-correlation energy is treated in the generalized gradient approximation (GGA) Perdew–Burke–Ernzerhof (PBE) [23]. Plane waves with an energy cutoff of 450 eV are used as the basis set for all the calculations. A Monkhorst-Pack Γ-centered $15\times7\times7$ k-point mesh is used for Brillouin zone sampling. The structure, including lattice parameters and atomic positions, are fully relaxed until the maximum residual ionic force is below 0.001 eV·Å^{-1}, and the total energy difference is converged to within 10^{-7} eV. The spin-orbit coupling (SOC) is included in our calculations.

3 Results and discussion

3.1 Crystal structure and electronic band structure

The crystal structure of Bi_2S_3 has a $Pmcn$ (#62) space group, which is different from other IV-VI compounds, such as Bi_2Te_3 [24] and Bi_2Se_3 [25], as shown in Fig. 1(a). Our theoretically relaxed lattice parameters are a = 11.178 Å, b = 11.809 Å and c = 4.016 Å, which is in good agreement with our experimental lattice parameters a = 11.150 Å, b = 11.322 Å and c = 3.988 Å (Table 2). It can be seen that the structure of Bi_2S_3 consists of two and three non-equivalent sites for Bi and S atoms, respectively. These five non-equivalent atoms formed a chain along c axis and zig-zag structure in the a–b plane. Each

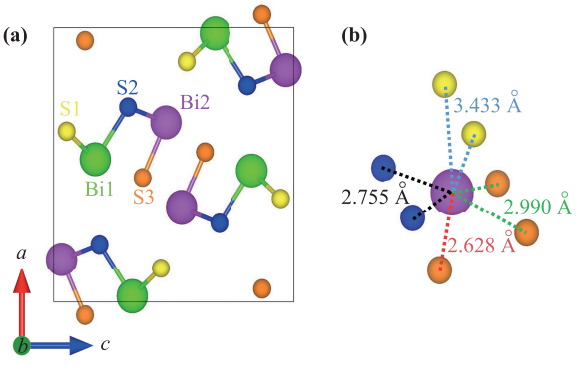

Fig. 1 **(a)** Crystal structure of Bi_2S_3. There are five non-equivalent atoms in unit cell and the green, pink, yellow, blue, and orange balls refer to Bi_1, Bi_2, S_1, S_2, S_3 atom, respectively. **(b)** Each Bi atom coordinated by seven S atoms, formed three short (black and red dashed lines) and four long bonds (green and blue dashed lines).

Table 2 Lattice parameters along a, b, c axis and volume of unit cell ($V = a \times b \times c$) of all samples studies in this work.

Samples	Compositions ($Bi_2S_{3-x-y}Se_xCl_y$)	a (Å)	b (Å)	c (Å)	V (Å^3)
$x = 0$, $y = 0\%$	undoped Bi_2S_3	11.150	11.322	3.9878	503.377
$x = 0.09$, $y = 0\%$	$Bi_2S_{2.91}Se_{0.09}$	11.166	11.326	3.9878	504.316
$x = 0.15$, $y = 0\%$	$Bi_2S_{2.85}Se_{0.15}$	11.170	11.335	3.9880	504.933
$x = 0.21$, $y = 0\%$	$Bi_2S_{2.79}Se_{0.21}$	11.172	11.351	3.9883	505.580
$x = 0.15$, $y = 0.15\%$	$Bi_2S_{2.8485}Se_{0.15}Cl_{0.0015}$	11.170	11.335	3.9880	504.933
$x = 0.15$, $y = 0.45\%$	$Bi_2S_{2.8455}Se_{0.45}Cl_{0.0045}$	11.168	11.332	3.9890	504.939
$x = 0.1$, $y = 0.75\%$	$Bi_2S_{2.8425}Se_{0.75}Cl_{0.0075}$	11.172	11.325	3.9905	504.892
$x = 0.15$, $y = 1.5\%$	$Bi_2S_{2.835}Se_{0.15}Cl_{0.015}$	11.174	11.322	3.9908	504.891
$x = 0.15$, $y = 3\%$	$Bi_2S_{2.82}Se_{0.15}Cl_{0.03}$	11.173	11.322	3.9913	504.889

Bi atom surrounded by seven S atoms and formed three short and four long bonds, as shown in Fig. 1(b). The calculated inter-chain chemical bond lengths are ~2.990–3.433 Å, smaller than the sum of covalent radii of Bi–S (~2.35 Å), indicating a typically weak interactions with some covalency. These weak couplings lead to a nonequilibrium force on Bi atom and cause significant phonon softening, as reported in layered SnS [7] and SnSe [26–28]. Considering the weak chemical bonding in the inter chain and strong phonon-orbital interactions, the low thermal conductivity can be anticipated in Bi_2S_3.

Figures 2(a) and (b) show the powder XRD patterns ranging from 10° to 80° for $Bi_2S_{3-x}Se_x$ (x = 0, 0.09, 0.15, 0.21) and $Bi_2S_{2.85-y}Se_{0.15}Cl_y$ (y = 0.0015, 0.0045, 0.0075, 0.015, 0.03). No impurity phases were observed in the XRD patterns, all peaks matching well to the orthorhombic Bi_2S_3 in the *Pmcn* space group. The lattice parameters for both $Bi_2S_{3-x}Se_x$ and $Bi_2S_{2.85-y}Se_{0.15}Cl_y$ samples are plotted visually in Figs. 2(c) and (d), and also listed in Table 2 along with the volume of unit cell. We observe that the lattice parameters slightly change along the three axes while the volume of unit cell increases firstly with adding Se content and then decreases slightly upon Cl doping. The expansion and shrinkage of crystal lattice

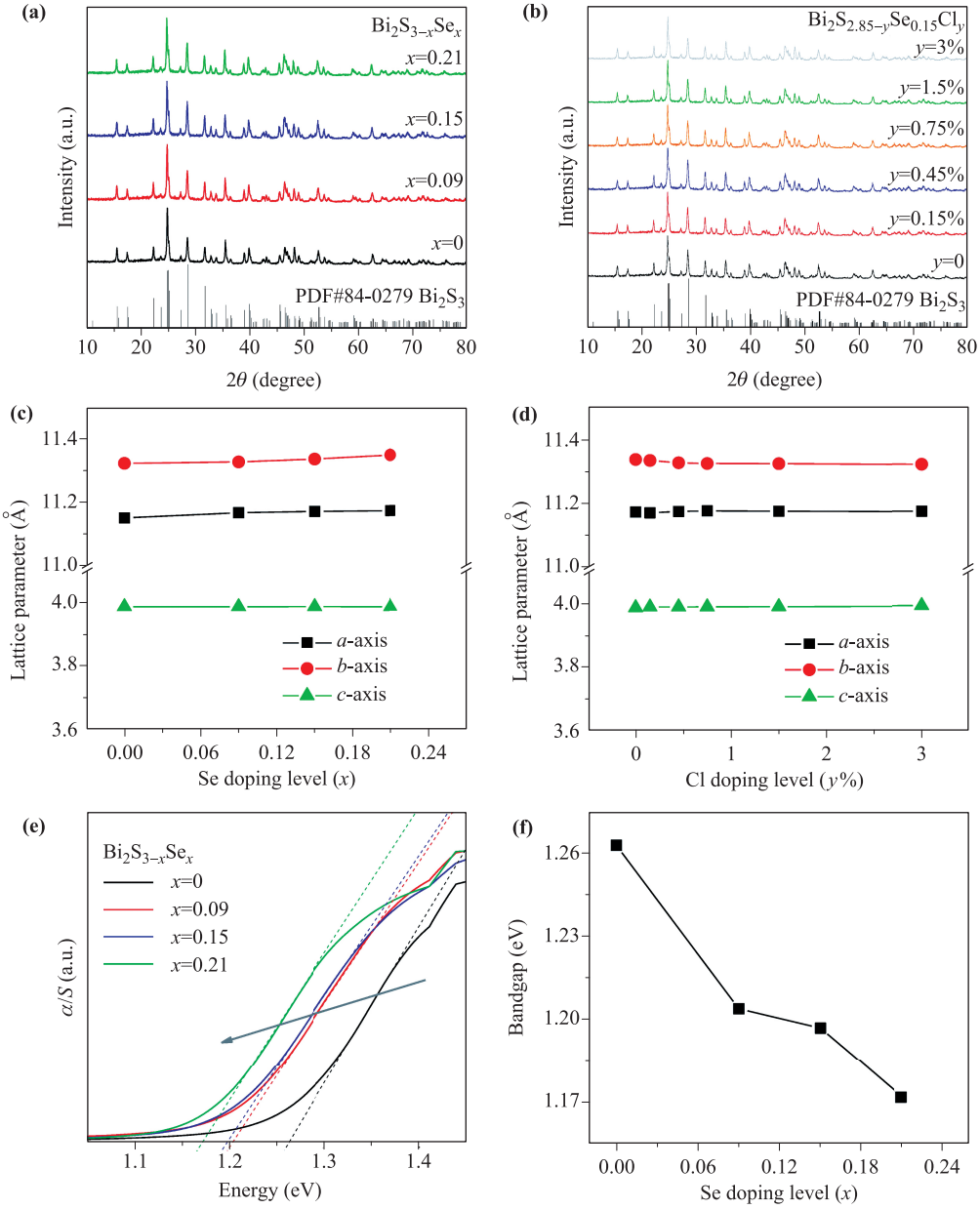

Fig. 2 Powder XRD patterns of **(a)** $Bi_2S_{3-x}Se_x$ (x = 0, 0.09, 0.15 and 0.21) and **(b)** $Bi_2S_{2.85-y}Se_{0.15}Cl_y$ (y = 0%, 0.15%, 0.45%, 0.75%, 1.5%, and 3%) samples; Lattice parameters of **(c)** $Bi_2S_{3-x}Se_x$ and **(d)** $Bi_2S_{2.85-y}Se_{0.15}Cl_y$ samples; **(e)** Electronic absorption spectra and **(f)** band gap values for $Bi_2S_{3-x}Se_x$ samples.

can be well explained by the difference in ionic radius of Se^{2-} (1.98 Å), Cl^{-} (1.84 Å) and S^{2-} (1.81 Å).

Figures 2(e) and (f) show the electronic absorption spectra of $Bi_2S_{3-x}Se_x$ powders and the band gap values obtained. According to the experiment data, the undoped Bi_2S_3 sample has a band gap of 1.26 eV, which is close to the reported values (1.30 eV [19, 20]). Upon Se alloying, the electronic absorption spectra of the $Bi_2S_{3-x}Se_x$ sample shows a continuous shift of the absorption edge toward lower energy. The band gap values keep decreasing from about 1.26 eV to 1.17 eV with Se doping level increased. Both XRD and band gap results indicate that Se and Cl are successfully introduced into the Bi_2S_3 lattice.

Figure 3 presents the calculated band structure and projected density of states (PDOS) of Bi_2S_3 with and without spin orbital coupling (SOC) effect considered. The calculated band gap with SOC effect is 1.03 eV [Fig. 3(a)], smaller than the experimentally measured 1.26 eV. However, a larger band gap 1.38 eV can be obtained without SOC, as shown in Fig. 3(b). Both the calculated band gaps consistent with experimental values reported to be 1.30–1.70 eV [29]. Though the DFT calculation does not give quantitatively accurate predictions of band gap, the trends of band between different bands are more reliable. Clearly, both the two methods validate the indirect band gap semiconductor. The valence band maximum (VBM) and the conduction band minimum (CBM) are located around Z point and along Γ-Y direction for both results with and without SOC, as shown in Figs. 3(a) and (b), which is consistent with previous reports [19, 29, 30]. An obvious hybrid effect can be seen in VBM and CBM from Figs. 3(c) and (d). The PDOS near VBM composed of Bi-6s, Bi-6p, and S-3p orbits [shown in Figs. 3(c) and (d)], and that near the CBM has Bi-6p, S-3s, and S-3p orbits [shown in inserted Figs. 3(c) and (d)] for both results with and without SOC.

3.2 Optimizing thermoelectric transport properties of n-type Bi_2S_3 via Se alloying

As an anisotropic layered material, we measured the thermoelectric transport properties along two different pressing directions for the SPSed Bi_2S_3 pellets. Figure 4 shows the temperature-dependent thermoelectric transport properties of undoped Bi_2S_3, the results show that the performance along the direction of parallel to the SPS pressing is superior. Thus, in the following text, we investigated and discussed the thermoelectric properties along the high performance direction.

As shown in Fig. 5(a), the undoped Bi_2S_3 sample shows

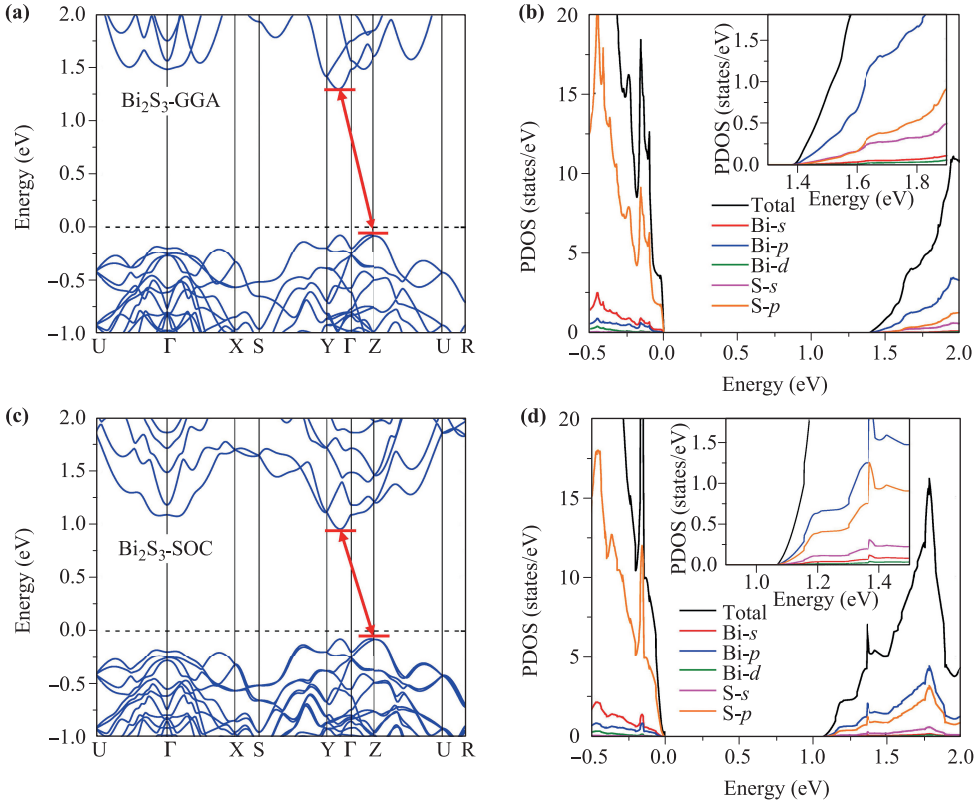

Fig. 3 Calculated electronic band structure **(a, c)** and projected density of states (PDOS) **(b, d)** for Bi_2S_3 with and without spin orbital coupling considered. The vertical red lines refer to valence band maximum (VBM) and conduction band minimum (CBM). The band gaps are 1.03 eV and 1.38 eV with and without SOC effect, respectively. The black dashed line refers to Fermi level. Inserted figures in (b) and (d) refer to enlarged energy window to focus on conduction band.

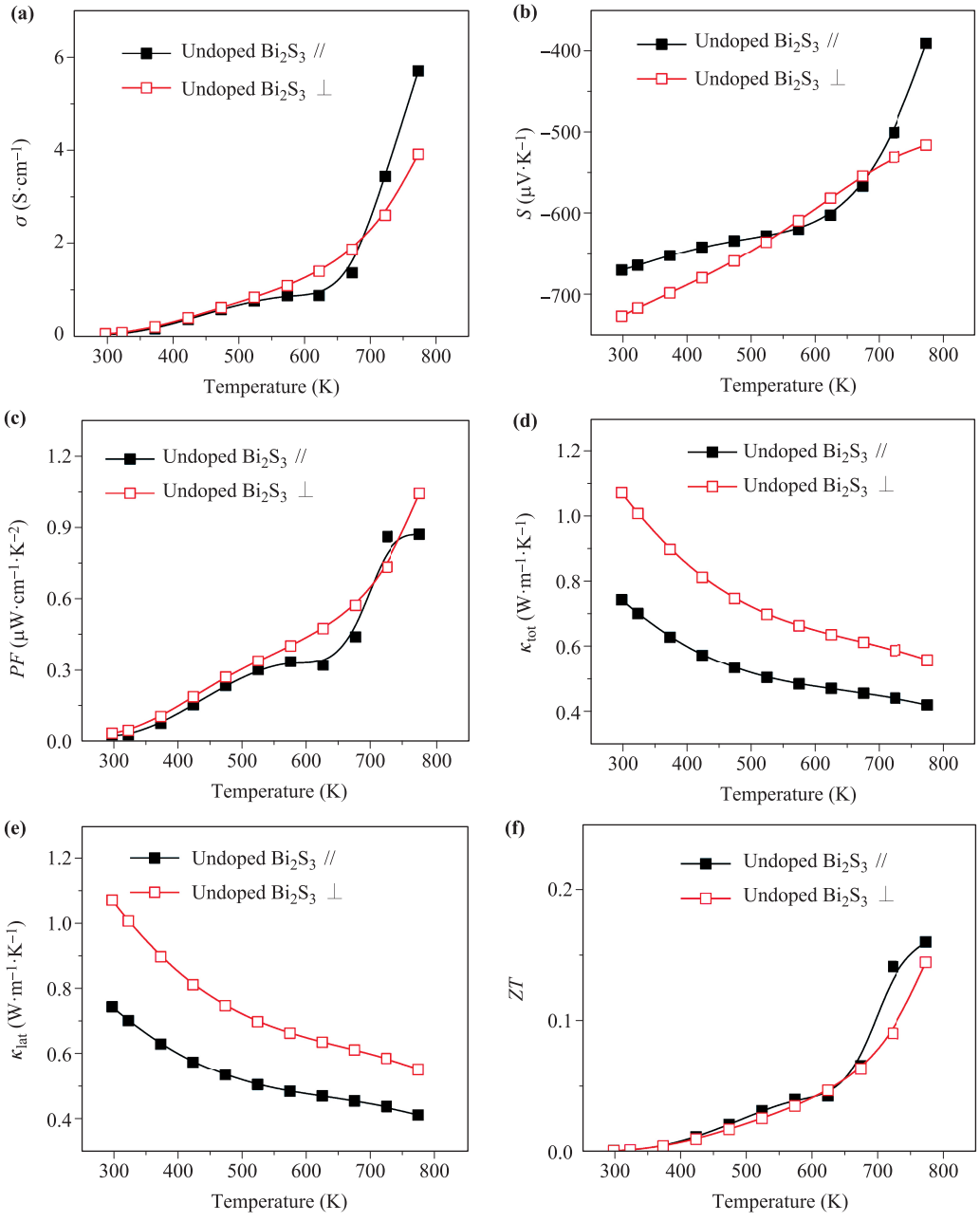

Fig. 4 Temperature-dependent **(a)** electrical conductivity (σ), **(b)** Seebeck coefficient (S), **(c)** power factor (σS^2), **(d)** total thermal conductivity (κ_{tot}), **(e)** lattice thermal conductivity (κ_{lat}), and **(f)** ZT values of undoped Bi_2S_3 sample along directions parallel and perpendicular to the SPS pressing direction.

very low electrical conductivity (σ) over the entire measurement range (300–773 K). The intrinsic low electrical conductivity is mainly due to the low carrier concentration ($\sim 9.8\times10^{16}$ cm^{-3}), as listed in Table 3. After Se alloying, the electrical transports are changed from semiconductor-like to metallic behaviors due to increasing carrier concentrations. Upon Se alloying, the temperature dependence of σ displays two distinct regions. At low temperature (<600 K), the electrical conductivity shows a nearly metallic behavior, linearly decreases with increasing temperature, resulting from the reduction of carrier mobility owing to the carrier-carrier scattering [15]. When the temperature increases, thermal activation of charge carriers greatly increases, which leads to further rising electrical conductivity [31]. Such transition from non-degenerate semiconductor behavior in undoped Bi_2S_3 to a nearly degenerate behavior could be explained by pushing Fermi levels into conduction band [31].

In Fig. 5(b), the negative Seebeck coefficient (S) indicates that all $Bi_2S_{3-x}Se_x$ samples ($x = 0, 0.09, 0.15, 0.21$) are n-type semiconductors. One can see that the temperature dependence of |S| displays an opposite tendency to

Table 3 Electrical transport properties of $Bi_2S_{3-x}Se_x$ samples where R_H, n_H, μ_H and σ is the hall coefficient, carrier concentration, hall mobility and electrical conductivity at room temperature, respectively.

Samples ($Bi_2S_{3-x}Se_x$)	R_H (RT) ($cm^3 \cdot C^{-1}$)	n_H (RT) (10^{17} cm^{-3})	μ_H (RT) ($cm^2 \cdot V^{-1} \cdot s^{-1}$)	σ (RT) ($S \cdot cm^{-1}$)
undoped Bi_2S_3	63.9	0.98	3.515	0.055
$x = 0.09$	4.04	15.4	26.01	6.439
$x = 0.15$	2.19	28.5	22.49	10.27
$x = 0.21$	5.16	12.1	24.70	4.787

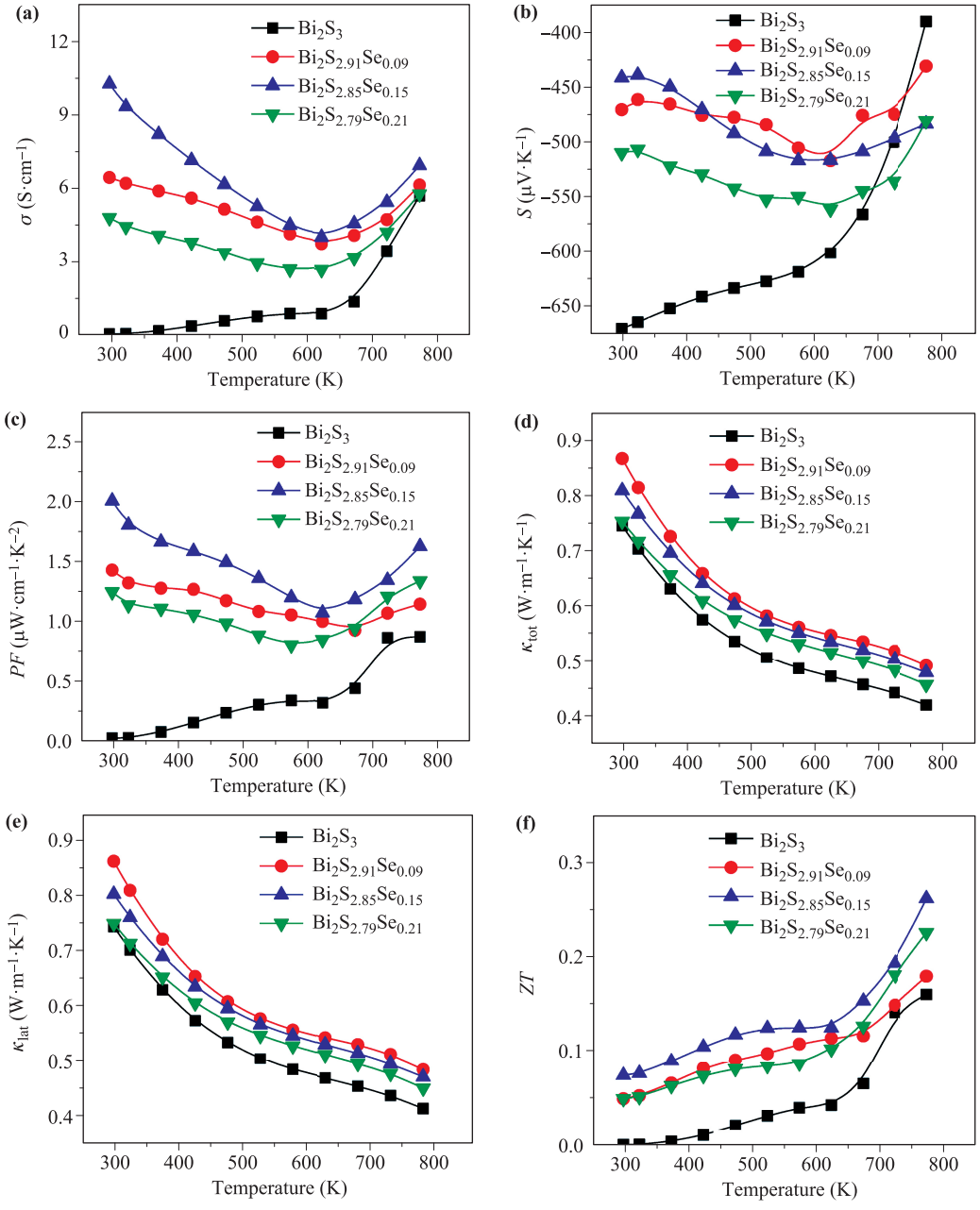

Fig. 5 Temperature-dependent **(a)** electrical conductivity (σ), **(b)** Seebeck coefficient (S), **(c)** power factor (σS^2), **(d)** total thermal conductivity (κ_{tot}), **(e)** lattice thermal conductivity (κ_{lat}), and **(f)** ZT values of $Bi_2S_{3-x}Se_x$ samples ($x = 0$, 0.09, 0.15, and 0.21).

the electrical conductivity with rising carrier concentrations. In Fig. 5(c), the highest power factor ($PF = \sigma S^2$) of 2.0 $\mu W \cdot cm^{-1} \cdot K^{-2}$ at room temperature was realized in the $Bi_2S_{2.85}Se_{0.15}$ sample, which is about 100 times higher than that of the undoped Bi_2S_3, the high PF values could be extended in the entire measurement temperature range.

Figures 5(d) and (e) show the temperature dependent total thermal conductivity (κ_{tot}) and lattice thermal conductivity ($\kappa_{lat} = \kappa_{tot} - \kappa_{ele}$) for $Bi_2S_{3-x}Se_x$ samples ($x = 0$, 0.09, 0.15, 0.21) samples, respectively. The temperature dependent thermal diffusivity and heat capacity data are shown in Fig. A1 and sample densities are shown in Table 1. The electronic thermal conductivity κ_{ele} is directly determined by σ with the Wiedemann–Franz law, $\kappa_{ele} = L \times \sigma \times T$, where L is the Lorenz number obtained by fitting the Seebeck coefficient to the reduced chemical potential [32]. The Lorentz number L and the electronic thermal conductivity κ_{ele} as a function of temperature are shown in Fig. A2. Obviously, the κ_{lat} displays almost the same values as κ_{tot} in the entire temperature range since the electronic thermal conductivity part is ignorable compared to lattice part. As displayed in Fig. 5(d), the κ_{tot} for all samples present the same decreasing trend while increasing temperature, indicating the phonon scattering is a dominant scattering mechanism. We observe that the κ_{tot} decreases from 0.81 $W \cdot m^{-1} \cdot K^{-1}$ at room temperature to 0.48 $W \cdot m^{-1} \cdot K^{-1}$ at 773 K in the $Bi_2S_{2.85}Se_{0.15}$ sample, which gives the highest ZT value of ~0.26 at 773 K [Fig. 5(f)].

3.3 Further optimizing thermoelectric transport properties for Se-alloyed Bi_2S_3 via Cl doping

Even though Se-alloying enhanced the carrier concentration up to $\sim 2.85 \times 10^{18}$ (Table 3) in the $Bi_2S_{2.85}Se_{0.15}$ sample, it is still far from the optimal order ($\sim 1.0 \times 10^{19}$ cm^{-3}) in a given thermoelectric system [2]. Therefore, we prepare n-type $Bi_2S_{2.85}Se_{0.15}$ samples using Cl as a donor to further optimize carrier concentration. No impurity phases were observed in the XRD patterns of $Bi_2S_{2.85-y}Se_{0.15}Cl_y$ ($y = 0$, 0.0015, 0.0045, 0.0075, 0.015, 0.03) samples as mentioned in Fig. 1.

Typically, the significant improvement of electrical conductivity (σ), as shown in Fig. 6(a), indicates that Cl as an effective donor can further improve the electron concentration in $Bi_2S_{2.85}Se_{0.15}$ (Table 4). One can see that the carrier concentration increases monotonously from 2.85×10^{18} cm^{-3} for of $Bi_2S_{2.85}Se_{0.15}$ to 6.58×10^{20} cm^{-3} in $Bi_2S_{2.82}Se_{0.15}Cl_{0.03}$. Regardless of the continuous decrease of carrier mobility after adding Cl content, the room-temperature electrical conductivity significantly increases from ~ 10 $S \cdot cm^{-1}$ for $Bi_2S_{2.85}Se_{0.15}$ to ~ 829 $S \cdot cm^{-1}$ for $Bi_2S_{2.82}Se_{0.15}Cl_{0.03}$. As shown in

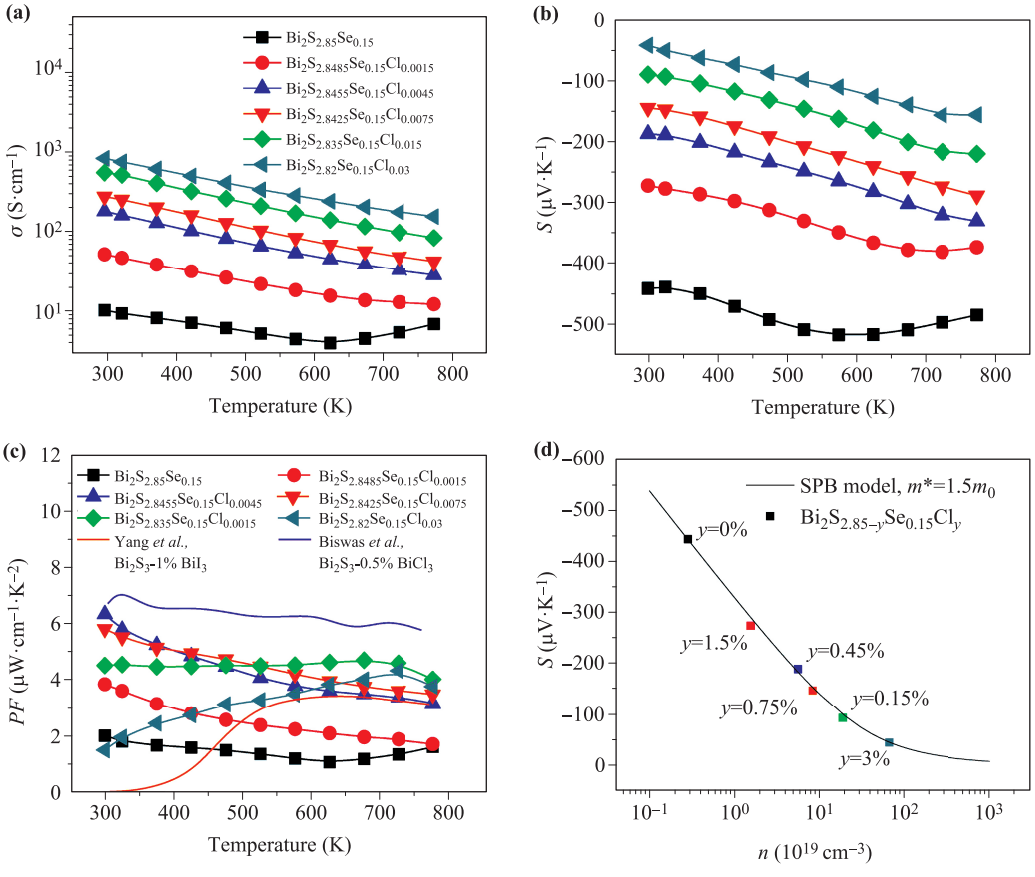

Fig. 6 Temperature-dependent electrical transport properties for $Bi_2S_{2.85-y}Se_{0.15}Cl_y$ samples ($y = 0\%$, 0.15%, 0.45%, 0.75%, 1.5% and 3%): **(a)** electrical conductivity (σ), **(b)** Seebeck coefficient (S) and **(c)** power factor (σS^2) compared with other high TE performance n-type Bi_2S_3-based materials [14, 16]; **(d)** Pisarenko plot shows the room temperature relationship of Seebeck coefficient and carrier concentration.

Table 4 Electrical transport properties of $Bi_2S_{2.85-y}Se_{0.15}Cl_y$ samples where R_H, n_H, μ_H and σ is the hall coefficient, carrier concentration, hall mobility and electrical conductivity at room temperature, respectively.

Samples ($Bi_2S_{2.85-y}Se_{0.15}Cl_y$)	R_H (RT) ($cm^3 \cdot C^{-1}$)	n_H (RT) (10^{19} cm^{-3})	μ_H (RT) ($cm^2 \cdot V^{-1} \cdot s^{-1}$)	σ (RT) ($S \cdot cm^{-1}$)
$y = 0\%$	219	0.29	22.49	10.27
$y = 0.15\%$	40.3	1.55	20.91	51.88
$y = 0.45\%$	11.2	5.57	20.25	180.5
$y = 0.75\%$	7.53	8.29	20.13	276.1
$y = 1.5\%$	3.34	18.7	18.39	550.6
$y = 3\%$	0.95	65.8	7.87	828.6

Fig. 6(b), with increasing Cl content, the absolute value of room temperature Seebeck coefficient keeps decreasing from 442 $\mu V \cdot K^{-1}$ for the $Bi_2S_{2.85}Se_{0.15}$ to 43 $\mu V \cdot K^{-1}$ for the $Bi_2S_{2.82}Se_{0.15}Cl_{0.03}$, indicating pronouncedly increasing carrier concentrations. As shown in Fig. 6(c), after further optimizing carrier concentration, PF was significantly improved and reaches a value of 6.3 $\mu W \cdot cm^{-1} \cdot K^{-2}$ at room temperature in $Bi_2S_{2.8455}Se_{0.15}Cl_{0.045}$, which is about 3 times higher than that in $Bi_2S_{2.85}Se_{0.15}$. The highest PF of 6.3 $\mu W \cdot cm^{-1} \cdot K^{-2}$ achieved in this study is comparable to Bi_2S_3 ingots [16] and even higher than I-doped Bi_2S_3 bulks [14].

Figure 6(d) shows the well-established Pisarenko relation between Seebeck coefficient and carrier concentration at room temperature. The black solid line is the Pisarenko line based on the single parabolic band (SPB) model with the effective mass $m^* = 1.5m_0$. In the case of a single parabolic band (SPB) [33], carrier concentration (n) and Seebeck coefficient (S) can be correlated as follows:

$$S = -\frac{k_B}{e}\left[\eta - \frac{(\lambda+2)F_{\lambda+1}(\eta)}{(\lambda+1)F_\lambda(\eta)}\right], \quad (1)$$

$$n = 4\pi\left(\frac{2m^*k_BT}{h^2}\right)^{3/2} F_\lambda(\eta), \quad (2)$$

where,

$$F_n(\eta) = \int_0^\infty \frac{x^n \mathrm{d}x}{1+\exp\ (x-\eta)}. \quad (3)$$

$F_n(\eta)$ is the Fermi integral calculated from specific reduced chemical potential, $\eta = E_F/(k_BT)$. Besides, h is Planck's constant, e is an electron charge and m^* is the effective mass of the charge carriers. At moderate temperature, electrons are scattered by acoustic phonon modes and $\lambda = 0$.

One can see that all Seebeck coefficients data of $Bi_2S_{2.85-y}Se_{0.15}Cl_y$ fall in the line, indicating that $Bi_2S_{2.85-y}Se_{0.15}Cl_y$ exhibits one single valence band transport, which is consistent with the band structure calculations in Fig. 3. Here, the effective mass of $1.5m_0$ is used in the SPB model plot, which matches surprisingly with the experimental results. The large effective mass of $1.5m_0$ is consistent with the large Seebeck coefficients in Bi_2S_3 system [11, 12, 14]. Our results also indicate that the validity of the single parabolic band model [34] and the negligible effects of Cl-doping on band structures [35].

The temperature dependent thermal transport properties of Cl-doped samples are shown in Fig. 7. The temperature dependent thermal diffusivity and heat capacity of $Bi_2S_{2.85-y}Se_{0.15}Cl_y$ (y = 0, 0.0015, 0.0045, 0.0075, 0.015, 0.03) samples are shown in Fig. A3 and the sample densities are shown in Table 1. The Lorentz number L and the electronic thermal conductivity κ_{ele} as a function of temperature are shown in Fig. A4. As Cl doping level rises, κ_{tot} exhibits an obvious increment in the entire temperature range, while κ_{lat} decreases

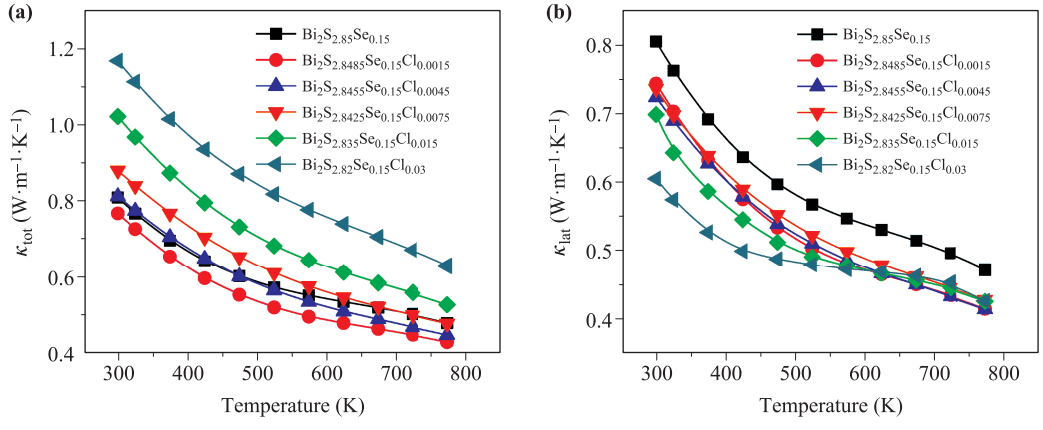

Fig. 7 Temperature-dependent thermal transport properties for $Bi_2S_{2.85-y}Se_{0.15}Cl_y$ samples (y = 0%, 0.15%, 0.45%, 0.75%, 1.5%, and 3%): **(a)** total thermal conductivity (κ_{tot}) and **(b)** lattice thermal conductivity (κ_{lat}).

from ~0.80 $W \cdot m^{-1} \cdot K^{-1}$ in $Bi_2S_{2.85}Se_{0.15}$ sample to ~0.60 $W \cdot m^{-1} \cdot K^{-1}$ for $Bi_2S_{2.82}Se_{0.15}Cl_{0.03}$ at 300 K. The reduction in lattice thermal conductivity may be related to the defects caused by introducing of Cl^- ions in the Bi_2S_3 lattice through heavily Cl doping, which need further clarifications.

Figure 8 shows the ZT values of $Bi_2S_{2.85-y}Se_{0.15}Cl_y$ samples as a function of temperature, other reported ZT and average ZT values are also plotted for comparison [14, 16]. As shown in Fig. 8(a), the thermoelectric figure of merit ZT is significantly enhanced, a maximum ZT value of 0.6 is achieved at 723 K in the $Bi_2S_{2.835}Se_{0.15}Cl_{0.015}$ sample *via* Se alloying and Cl doping. One can see in Figs. 8(b) and (c) that the highest ZT and average ZT value of $Bi_2S_{2.835}Se_{0.15}Cl_{0.015}$ sample in this work are comparable or even higher than other high performance n-type Bi_2S_3-based materials [14, 16].

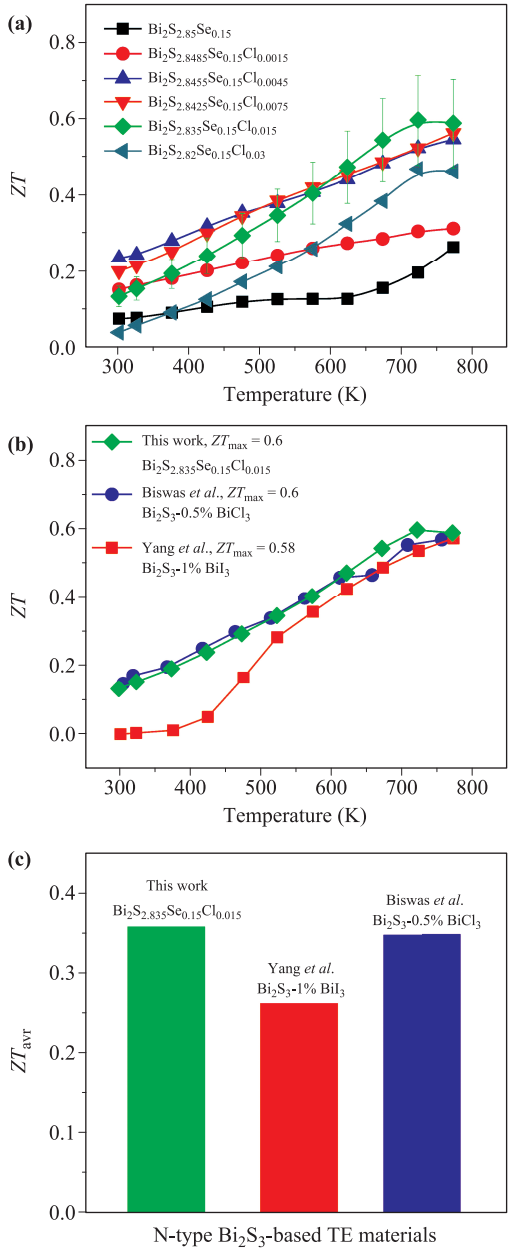

Fig. 8 **(a)** ZT values as a function of temperature for $Bi_2S_{2.85-y}Se_{0.15}Cl_y$ samples (y = 0%, 0.15%, 0.45%, 0.75%, 1.5%, and 3%); **(b)** ZT values and **(c)** average ZT for $Bi_2S_{2.835}Se_{0.15}Cl_{0.015}$ sample in comparison with other high TE performance n-type Bi_2S_3-based materials [14, 16].

4 Conclusions

In this work, we successfully synthesized n-type Bi_2S_3-based thermoelectric materials via Se alloying and Cl doping using melting and SPS process. Our results indicate that Se-alloying can effectively narrow the band gap and increase the carrier concentration for Bi_2S_3. Furthermore, Cl doping can significantly improve the electrical transport properties of Bi_2S_3 system through optimizing carrier concentration. Se alloying and Cl doping considerably enhance the power factor, combining with lowering lattice thermal conductivity leads to a maximum ZT value of ~0.6 at 723 K in $Bi_2S_{2.835}Se_{0.15}Cl_{0.015}$ sample. A higher thermoelectric performance is expected in Bi_2S_3 system when the approaches of nanostructuring or band structure engineering, or advanced processing methods are applied.

Acknowledgements This work was supported by the National Key Research and Development Program of China under Grant No. 2018YFB0703600, the National Natural Science Foundation of China under Grant Nos. 51772012, 51671015, and 51571007, the Beijing Municipal Science & Technology Commission under Grant No. Z171100002017002, the Shenzhen Peacock Plan team under Grant No. KQTD2016022619565991, and 111 Project under Grant No. B17002. This work was also supported by the High Performance Computing Center of Henan Normal University.

References

1. C. Chang, M. Wu, D. He, Y. Pei, C. F. Wu, X. Wu, H. Yu, F. Zhu, K. Wang, Y. Chen, L. Huang, J. F. Li, J. He, and L. D. Zhao, 3D charge and 2D phonon transports leading to high out-of-plane ZT in n-type SnSe crystals, *Science* 360(6390), 778 (2018)

2. G. Tan, L. D. Zhao, and M. G. Kanatzidis, Rationally designing high-performance bulk thermoelectric materials, *Chem. Rev.* 116(19), 12123 (2016)

3. Z. H. Ge, B. P. Zhang, P. P. Shang, Y. Q. Yu, C. Chen, and J. F. Li, Enhancing thermoelectric properties of polycrystalline Bi_2S_3 by optimizing a ball-milling process, *J. Electron. Mater.* 40(5), 1087 (2011)

4. L.-D. Zhao, S.-H. Lo, Y. Zhang, H. Sun, G. Tan, C. Uher, C. Wolverton, V. P. Dravid, and M. G. Kanatzidis, Ultralow thermal conductivity and high thermoelectric figure of merit in SnSe crystals, *Nature 508* (7496), 373 (2014)

5. X. Zhang, D. Wang, H. Wu, M. Yin, Y. Pei, S. Gong, L. Huang, S. J. Pennycook, J. He, and L. D. Zhao, Simultaneously enhancing the power factor and reducing the thermal conductivity of SnTe via introducing its analogues, *Energy Environ. Sci.* 10(11), 2420 (2017)
6. Y. M. Zhou, H. J. Wu, Y. L. Pei, C. Chang, Y. Xiao, X. Zhang, S. K. Gong, J. Q. He, and L. D. Zhao, Strategy to optimize the overall thermoelectric properties of SnTe via compositing with its property-counter $CuInTe_2$, *Acta Mater.* 125, 542 (2017)
7. W. He, D. Wang, J. F. Dong, Y. Qiu, L. Fu, Y. Feng, Y. Hao, G. Wang, J. Wang, C. Liu, J. F. Li, J. He, and L. D. Zhao, Remarkable electron and phonon band structures lead to a high thermoelectric performance $ZT > 1$ in earth-abundant and eco-friendly SnS crystals, *J. Mater. Chem. A* 6(21), 10048 (2018)
8. Z. H. Ge, L. D. Zhao, D. Wu, X. Liu, B. P. Zhang, J. F. Li, and J. He, Low-cost, abundant binary sulfides as promising thermoelectric materials, *Mater. Today* 19(4), 227 (2016)
9. Y. Kawamoto and H. Iwasaki, Thermoelectric properties of $(Bi_{1-x}Sb_x)_2S_{-3}$ with orthorhombic structure, *J. Electron. Mater.* 43(6), 1475 (2014)
10. B. Chen, C. Uher, L. Iordanidis, and M. G. Kanatzidis, Transport properties of Bi_2S_3 and the ternary bismuth sulfides $KBi_{6.33}S_{10}$ and $K_2Bi_8S_{13}$, *Chem. Mater.* 9(7), 1655 (1997)
11. Z. Liu, Y. Pei, H. Geng, J. Zhou, X. Meng, W. Cai, W. Liu, and J. Sui, Enhanced thermoelectric performance of Bi_2S_3 by synergistical action of bromine substitution and copper nanoparticles, *Nano Energy* 13, 554 (2015)
12. Z. H. Ge, B. P. Zhang, Y. Liu, and J. F. Li, Nanostructured $Bi_{2-x}Cu_xS_3$ bulk materials with enhanced thermoelectric performance, *Phys. Chem. Chem. Phys.* 14(13), 4475 (2012)
13. Y. Q. Yu, B. P. Zhang, Z. H. Ge, P. P. Shang, and Y. X. Chen, Thermoelectric properties of Ag-doped bismuth sulfide polycrystals prepared by mechanical alloying and spark plasma sintering, *Mater. Chem. Phys.* 131(1–2), 216 (2011)
14. J. Yang, G. Liu, J. Yan, X. Zhang, Z. Shi, and G. Qiao, Enhanced the thermoelectric properties of n-type Bi_2S_3 polycrystalline by iodine doping, *J. Alloys Compd.* 728, 351 (2017)
15. X. Du, F. Cai, and X. Wang, Enhanced thermoelectric performance of chloride doped bismuth sulfide prepared by mechanical alloying and spark plasma sintering, *J. Alloys Compd.* 587, 6 (2014)
16. K. Biswas, L. D. Zhao, and M. G. Kanatzidis, Tellurium-free thermoelectric: The anisotropic n-type semiconductor Bi_2S_3, *Adv. Energy Mater.* 2(6), 634 (2012)
17. L. J. Zhang, B. P. Zhang, Z. H. Ge, and C. G. Han, Fabrication and properties of $Bi_2S_{3-x}Se_x$ thermoelectric polycrystals, *Solid State Commun.* 162, 48 (2013)
18. W. Liu, K. C. Lukas, K. McEnaney, S. Lee, Q. Zhang, C. P. Opeil, G. Chen, and Z. Ren, Studies on the Bi_2Te_3-Bi_2Se_3-Bi_2S_3 system for mid-temperature thermoelectric energy conversion, *Energy Environ. Sci.* 6(2), 552 (2013)
19. J. Pei, L. J. Zhang, B. P. Zhang, P. P. Shang, and Y. C. Liu, Enhancing the thermoelectric performance of $Ce_xBi_2S_3$ by optimizing the carrier concentration combined with band engineering, *J. Mater. Chem. C* 5(47), 12492 (2017)
20. L. D. Zhao, B. P. Zhang, W. S. Liu, H. L. Zhang, and J. F. Li, Enhanced thermoelectric properties of bismuth sulfide polycrystals prepared by mechanical alloying and spark plasma sintering, *J. Solid State Chem.* 181(12), 3278 (2008)
21. P. E. Blöchl, Projector augmented-wave method, *Phys. Rev. B* 50(24), 17953 (1994)
22. G. Kresse and J. Furthmüller, Efficient iterative schemes for ab initio total-energy calculations using a plane-wave basis set, *Phys. Rev. B* 54(16), 11169 (1996)
23. J. P. Perdew, K. Burke, and M. Ernzerhof, Generalized gradient approximation made simple, *Phys. Rev. Lett.* 77(18), 3865 (1996)
24. L. D. Zhao, B. P. Zhang, J. F. Li, H. L. Zhang, and W. S. Liu, Enhanced thermoelectric and mechanical properties in textured n-type Bi_2Te_3 prepared by spark plasma sintering, *Solid State Sci.* 10(5), 651 (2008)
25. R. Larson, V. A. Greanya, W. C. Tonjes, R. Liu, S. D. Mahanti, and C. G. Olson, Electronic structure of Bi_2X_3 (X=S, Se, T) compounds: Comparison of theoretical calculations with photoemission studies, *Phys. Rev. B* 65(8), 085108 (2002)
26. L. D. Zhao, S. H. Lo, Y. Zhang, H. Sun, G. Tan, C. Uher, C. Wolverton, V. P. Dravid, and M. G. Kanatzidis, Ultralow thermal conductivity and high thermoelectric figure of merit in SnSe crystals, *Nature* 508(7496), 373 (2014)
27. Y. Xiao, C. Chang, Y. L. Pei, D. Wu, K. L. Peng, X. Y. Zhou, S. K. Gong, J. Q. He, Y. S. Zhang, Z. Zeng, and L. D. Zhao, Origin of low thermal conductivity in SnSe, *Phys. Rev. B* 94(12), 125203 (2016)
28. L. D. Zhao, G. Tan, S. Hao, J. He, Y. Pei, H. Chi, H. Wang, S. Gong, H. Xu, V. P. Dravid, C. Uher, G. J. Snyder, C. Wolverton, and M. G. Kanatzidis, Ultrahigh power factor and thermoelectric performance in hole-doped single-crystal SnSe, *Science* 351(6269), 141 (2016)
29. R. Chmielowski, D. Péré, C. Bera, I. Opahle, W. Xie, S. Jacob, F. Capet, P. Roussel, A. Weidenkaff, G. K. H. Madsen, and G. Dennler, Theoretical and experimental investigations of the thermoelectric properties of Bi_2S_3, *J. Appl. Phys.* 117(12), 125103 (2015)
30. P. Larson, V. A. Greanya, W. C. Tonjes, R. Liu, S. D. Mahanti, and C. G. Olson, Electronic structure of Bi_2X_3 (X=S, Se, T) compounds: Comparison of theoretical calculations with photoemission studies, *Phys. Rev. B* 65(8), 085108 (2002)
31. K. Peng, X. Lu, H. Zhan, S. Hui, X. Tang, G. Wang, J. Dai, C. Uher, G. Wang, and X. Zhou, Broad temperature plateau for high ZTs in heavily doped p-type SnSe single crystals, *Energy Environ. Sci.* 9(2), 454 (2016)

32. L. D. Zhao, S. H. Lo, J. He, H. Li, K. Biswas, J. Androulakis, C. I. Wu, T. P. Hogan, D. Y. Chung, V. P. Dravid, and M. G. Kanatzidis, High performance thermoelectrics from earth-abundant materials: Enhanced figure of merit in PbS by second phase nanostructures, *J. Am. Chem. Soc.* 133(50), 20476 (2011)

33. H. Wu, C. Chang, D. Feng, Y. Xiao, X. Zhang, Y. Pei, L. Zheng, D. Wu, S. Gong, Y. Chen, J. He, M. G. Kanatzidis, and L. D. Zhao, Synergistically optimized electrical and thermal transport properties of SnTe via alloying high-solubility MnTe, *Energy Environ. Sci.* 8(11), 3298 (2015)

34. K. Imasato, S. D. Kang, S. Ohno, and G. J. Snyder, Band engineering in Mg_3Sb_2 by alloying with Mg_3Bi_2 for enhanced thermoelectric performance, *Mater. Horiz.* 5(1), 59 (2018)

35. Y. Xiao, H. Wu, W. Li, M. Yin, Y. Pei, Y. Zhang, L. Fu, Y. Chen, S. J. Pennycook, L. Huang, J. He, and L. D. Zhao, Remarkable roles of Cu to synergistically optimize phonon and carrier Transport in n-Type PbTe-Cu_2Te, *J. Am. Chem. Soc.* 139(51), 18732 (2017)